Received: 6 January 2025 | Revised: 7 April 2026 | Accepted: 10 April 2026
DOI: 10.33012/navi.770

ORIGINAL ARTICLE

Augmenting GNSS with LEO-PNT and 5G for Enhanced Positioning in Urban Environments

Marianna Alghisi[1] | **Florin-Catalin Grec**[2] | **Raul Orus Perez**[2] | **Ludovico Biagi***[1]

[1] DICA Politecnico di Milano, Piazza Leonardo Da Vinci 32, 20133 Milano, Italy
[2] European Space Agency, Keplerlaan 1, 2201AZ Noordwijk, The Netherlands

Correspondence
*Ludovico Biagi
DICA Politecnico di Milano,
Piazza Leonardo Da Vinci 32,
20133 Milano, Italy.
Email: ludovico.biagi@polimi.it

Abstract
Global navigation satellite systems (GNSSs) are the only global, free, comprehensive technology providing absolute and accurate positioning, navigation, and timing (PNT) services to users worldwide. These services have become an indispensable part of modern society, playing a critical role in many commercial, industrial, scientific, and safety-critical applications. Numerous applications, including mass marketing, professional, and other applications linked to critical infrastructure, heavily depend on GNSSs, with increased expectations for more reliability, accuracy, and availability. However, in specific scenarios, the number of visible satellites can be low, even when all GNSS constellations are used: this is the case, for example, in urban environments or mountain terrain, where the position accuracy can be poor or position estimation may not even be possible. In such cases, the integration of a GNSS with other positioning technologies, such as 5G, and the low Earth orbit (LEO)-PNT concept could improve results. Over the last years, LEO satellites have been put in orbit for several purposes such as telecommunication and Earth observation. Now, several private and institutional actors are considering the idea of designing and deploying LEO satellites for PNT services, by equipping these satellites with payloads able to transmit signals with a design that is interoperable with those already broadcasted by GNSS satellites. Therefore, the aim of this work is to assess the possible integration of GNSS (and 5G) with LEO-PNT positioning signals. Real-life GNSS and 5G data are used from a previous experiment, conducted in the fall of 2023 in northern Italy. LEO-PNT orbits are generated and provided by the European Space Agency. LEO visibility tables and pseudorange observations are simulated for a given location and date. The measurements are combined and processed in a tightly coupled extended Kalman filter, and results are generated for different configurations: 5G standalone, GNSS standalone, LEO-PNT standalone, LEO-PNT + 5G, and GNSS + LEO-PNT. Among these cases, the integrated GNSS + LEO-PNT solution provides the best results.

Keywords
5G, GNSS, LEO-PNT

1 | INTRODUCTION

To overcome global navigation satellite system (GNSS) weaknesses—such as signal obstruction by buildings, vulnerability to interference and jamming (Zhu et al., 2018), and poor indoor availability (Farahsari et al., 2022)—significant efforts have been made in recent years to develop alternative and complementary positioning technologies. Terrestrial-based positioning using telecommunication networks has gained considerable attention, particularly with the advent of 5G (Dwivedi et al., 2021; Fisher, 2021). This technology has enabled innovative approaches to precision navigation through the introduction of dedicated positioning signals (e.g., positioning reference signals [PRSs], sounding reference signals [SRSs]), higher frequency bands, wideband signals, and beamforming techniques (Italiano et al., 2024). These advancements are expected to enhance navigation capabilities in urban environments, where GNSS performance is impaired by the built environment, improving signal geometry and the overall availability of positioning systems (Alghisi & Biagi, 2023). Nevertheless, implementing accurate positioning services in 5G networks is not a trivial process. First, although dense infrastructure deployment is beneficial for positioning, it can introduce significant inter-station interference, negatively affecting data throughput and proving costly for operators—especially in the absence of a viable commercial business case. Second, the inherent design of 5G networks prioritizes communication efficiency over positioning accuracy, meaning that the architecture is not optimized for localization. As a result, a highly capable communication system does not necessarily equate to an effective positioning system, despite all of the capabilities specified by the Third Generation Partnership Project (3GPP) in recent years (Chaloupka, 2017).

Numerous studies have investigated 5G positioning performance based on simulated or synthetic observations (del Peral-Rosado et al., 2018; Mata et al., 2020; Pileggi et al., 2023). The evaluation of 5G positioning using field measurements is still in its early stages and remains an active area of research. Many challenges encountered in actual deployment—such as network synchronization and signal interference—still need to be fully understood and assessed. However, several recent studies have begun to address this gap through experimental investigations (Abdallah & Kassas, 2022; Shahcheraghi, Kuric, et al., 2024). The history of positioning in cellular networks began in the mid-1990s with the introduction of long-term evolution (LTE) technology in 3GPP Release 9, in order to meet emergency call positioning regulations. Network-assisted GNSS and downlink positioning were added to comply with the United States Federal Communications Commission's 911 requirements (FCC, 1996), enabling dispatchers to access cell phone location data during emergencies. Although significant progress has been made only in recent years in the field of cellular positioning, new possibilities have emerged owing to the advent of 5G technology. Figure 1 briefly summarizes the major advancements in 5G positioning introduced by 3GPP according to the latest releases. In particular, between 2016 and 2022, cellular positioning advanced significantly with the development of 5G New Radio (NR) technology (Vook et al., 2018), expanding its use to possible commercial applications (Wymeersch et al., 2017).

In addition to 5G, the concept of low Earth orbit (LEO) positioning, navigation, and timing (PNT) has rapidly advanced in recent years through both private (e.g., Centispace (Li et al., 2024), Xona Space (Singh, 2023)) and institutional (e.g., European Space Agency [ESA]) initiatives. LEO constellations can significantly enhance PNT services owing to their geometric diversity and improved satellite–user equipment (UE) geometry. Moreover, their lower orbital altitudes

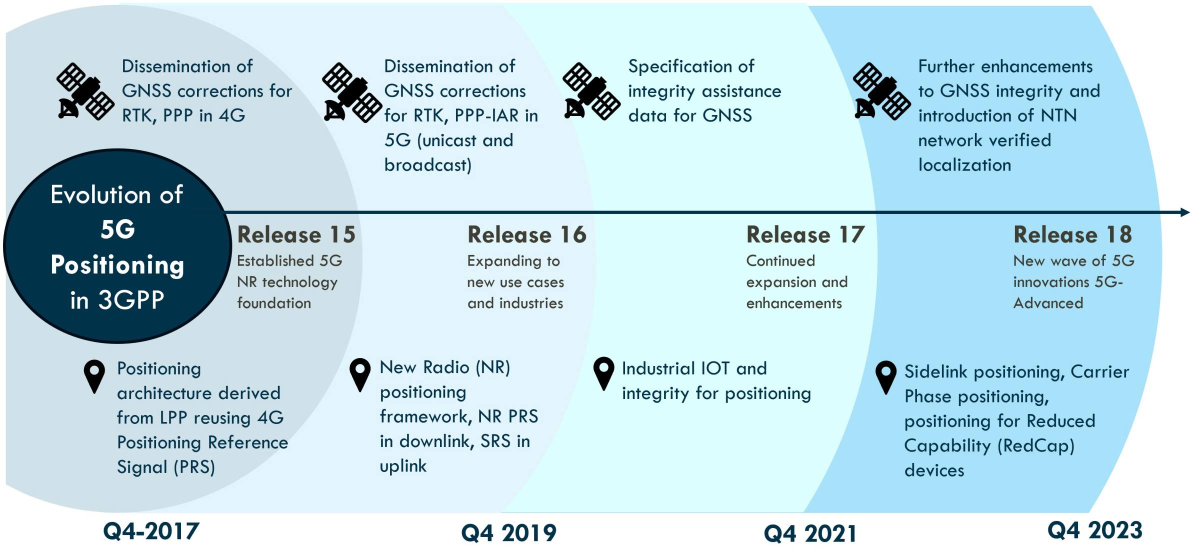

FIGURE 1 Timeline of NR positioning in 3GPP
IAR: integer ambiguity resolution; IOT: internet of things; LPP: LTE positioning protocol; NTN: non-terrestrial network

reduce free-space losses and atmospheric disturbances, offering the potential for improved reliability and performance in challenging environments through stronger signals (Li et al., 2022; Prol et al., 2023; Ries et al., 2023). The aim of this work is to investigate the effectiveness of a hybrid positioning solution that integrates real GNSS and 5G pseudoranges (code observations) with synthetic LEO observations (no data from a LEO-PNT system are available at the time of this research). The analysis focuses on urban scenarios, where positioning performance is degraded by reduced satellite visibility. A partially obstructed scenario is simulated by applying a 20° cutoff. It is worth mentioning that we use real GNSS and 5G observations, measured in an industrial area, that capture the effects of multipath, signal blockage, and non-line-of-sight reception. In contrast, the LEO observations are simulated and do not include multipath. These limitations will be addressed in future work, where more detailed urban propagation models for LEO constellations will be considered.

This paper aims to investigate the possible improvements in positioning obtained by integrating GNSS, 5G, and LEO satellites. In a recent paper (Brambilla et al., 2024), the authors conducted an experiment on the integration of GNSS with 5G. That prior paper detailed the algorithms and implementation of an integrated solution; moreover, experimental data were collected and used to test the solutions. In the present paper, these data are integrated with LEO data. By emulating the geometry of a LEO constellation at the location of the UE where 5G and GNSS observations were recorded, we generate realistic satellite data. These data connect simulated observations with real measurements, adjusted via the receiver's GNSS clock and tropospheric delay computations. This approach allows the simulation of a scenario where a receiver tracks both signal sources coherently. Observations are jointly processed using an extended Kalman filter (EKF), considering different integration scenarios. Results demonstrate that the positioning accuracy can be significantly improved, reaching meter-level precision, even with only 3–4 LEO satellites in view, compared with standalone solutions using either 5G positioning or GNSS code-based positioning. The present paper discusses the following innovative aspects:

1. A possible future constellation of LEO-PNT satellites is hypothesized; the relevant orbits are simulated.
2. Based on the LEO satellites, a methodology and relevant software are studied and developed to simulate LEO pseudorange observations.
3. Algorithms and code are studied and developed for a joint processing of GNSS and LEO pseudoranges, together with 5G time of arrival (TOA), through an EKF.
4. All of the developed algorithms are tested via observations collected in the field for GNSS and 5G, with simulations utilized for LEO-PNT.

This paper is organized as follows: Section 2 presents the positioning models for the GNSS, 5G, and LEO. Then, the adopted methodology and the implemented EKF are described. Section 3 briefly discusses the experimental data and the simulation of LEO observations. Section 4 presents the results obtained by individual (5G, GNSS, or LEO only) solutions, as well as the results obtained by integrating 5G or GNSS with LEO.

2 | POSITIONING MODELS

In this work, the term "GNSS" refers to all satellite-based systems able to provide global positioning services. The main global operational systems include the United States' Global Positioning System (GPS), the European Union's Galileo, China's BeiDou Navigation Satellite System, and Russia's Global Navigation Satellite System (GLONASS). GNSS satellites typically transmit two types of ranging measurements: code and phase observations. Code observations measure the time delay of the pseudorandom noise code transmitted by the satellite to the receiver, representing the pseudodistance between the satellite and receiver. This distance is obtained by calculating the time shift between the received signal and an internal replica generated within the receiver, with the measurement expressed in meters. The carrier phase observations refer to the measurement of the carrier wave phase shift between the satellite signal and the receiver, measured in cycles. Phase observations are highly accurate, often achieving millimeter- to centimeter-level precision, but they require more complex processing compared with code observations; moreover, positioning based on phases is also vulnerable to cycle slips and loss-of-lock events, which interrupt the tracking and require ambiguity re-initialization.

In this work, we focus exclusively on GNSS and LEO-PNT code observations as an initial step, laying the groundwork before progressing to more advanced algorithms that incorporate carrier phase measurements and integer ambiguity resolution.

In the following, we report—according to the standard literature (Leick et al., 2015; Teunissen & Montenbruck, 2017)—the code observation equation of a measurement from satellite s tracked by receiver UE at epoch t, where s belongs to GNSS constellation S and the code signal is modeled on frequency $f = 1, \ldots, j$:

$$P_{UE}^{s,f}(t) = \rho_{UE}^{s}(t) + T_{UE}^{s}(t) + I_{UE}^{s,f}(t) + c(dt_{UE}(t) + d_{UE}^{S,f} - dt^{s,f}(t)) + \nu(t) \tag{1}$$

where:

- ρ_{UE}^{s} is the distance of the user from satellite s.
- T_{UE}^{s} is the tropospheric delay between satellite s and the UE.
- I_{UE}^{s} is the ionospheric delay between satellite s and the UE.

- dt_{UE} is the clock bias of the UE.
- $d_{UE}^{S,f}$ is the hardware bias of the UE, which is different for each constellation and each frequency.
- $dt^{s,f}$ is the bias of satellite s on frequency f, including clock and hardware.
- v is the measurement noise.

The adopted notation is based on the standard literature (Teunissen & Montenbruck, 2017).

It is well known that when a multi-frequency receiver is used, it is possible to combine observations from a single satellite s on two different frequencies. A specific combination of observations is known as the ionosphere-free combination, which yields a single observation for satellite s that is free of ionospheric disturbance. Considering an epoch t and two observations from satellite s on frequencies A and B, it is possible to calculate the corresponding ionosphere-free observation as follows:

$$P_{UE,IF}^{s}(t) = \alpha_A P_{UE}^{s,A} + \alpha_b P_{UE}^{s,B} \tag{2}$$

where the coefficients α_A and α_B depend on the frequency values. In this work, GNSS code observations are processed in the ionosphere-free combination, and we assume to have one $d_{UE}^{S,f}$ per each processed GNSS constellation (namely, GPS, Galileo, and BeiDou). By combining Equations (1) and (2), we obtain the ionosphere-free observation equation:

$$P_{UE,IF}^{s}(t) = \rho_{UE}^{s}(t) + T_{UE}^{s}(t) + c(dt_{UE}(t) + d_{UE}^{S,IF} - dt^{s,IF}(t)) + v(t) \tag{3}$$

In GNSS standard code processing, the tropospheric delay can be modeled with standard models available from the literature (Hobiger & Jakowski, 2017). This could leave some residual bias that is considered part of the final error budget. Moreover, in the processing, the clock offset and hardware biases of the receiver are typically grouped: $dt_{UE}(t) + d_{UE}^{S,IF} = d_{UE}^{S,IF}(t)$; thus, one general bias (clock + hardware) must be estimated for each epoch and constellation.

2.1 | 5G Positioning

According to 3GPP Release 16, a new positioning protocol and new positioning methods are introduced in 5G, including the dissemination of precise GNSS corrections (e.g., precise point positioning [PPP] and PPP real-time kinematics [RTK]) and downlink and uplink pilot allocations for positioning (3rd Generation Partnership Project (3GPP), 2017). New positioning signals are also introduced: downlink PRSs and uplink SRSs (3rd Generation Partnership Project (3GPP), 2020b). Specifically, the PRS allows for TOA estimation at the UE from multiple base stations (BSs), supporting TOA-based trilateration to determine the unknown position of the user node, as illustrated in Figure 2. This localization method relies on time measurements transmitted through BS radio signals within the 5G network, utilizing the time-of-flight principle. Here, the measured time interval is converted to distance through multiplication by the speed of light, c. A fundamental prerequisite for the effectiveness of this method is the precise synchronization of the BSs within the 5G network. This remains a significant challenge in real-life deployments, as maintaining accurate time synchronization on the order of a few tenths of nanoseconds

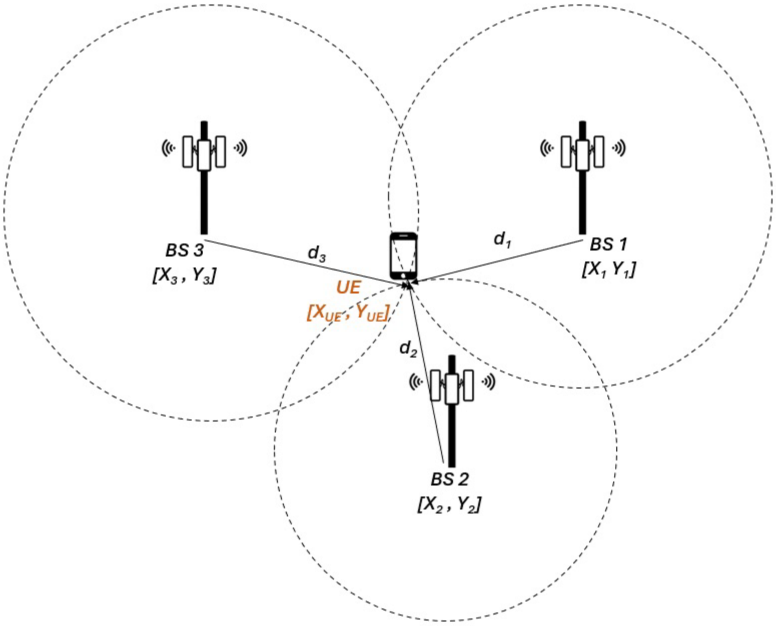

FIGURE 2 5G positioning: UE localization with TOA

is required for ranging measurements—although not necessarily for communication services (Koivisto et al., 2017; Ruffini et al., 2021; Tedeschini et al., 2023).

Assuming that the BSs and the UE have synchronized clocks, a signal transmitted by the i-th BS at time T_{Tx} is received at the UE at time T_{Rx}. On the UE side, it is possible to compute the time of flight, τ, by subtracting the signal transmission time from the arrival time. The noise-free distance $d_{UE}^{BS_i}$ from the i-th transmitting point to the target UE can be obtained by multiplying the time of flight by the speed of light c:

$$\begin{aligned} \tau_{UE}^{BS\ i} &= T_{Rx} - T_{Tx}^{BS\ i}, \quad \forall i \in \{1, 2, \ldots, M\} \\ \rho_{UE}^{BS\ i} &= \tau_{UE}^{BS\ i} * c, \quad \forall i \in \{1, 2, \ldots, M\} \end{aligned} \tag{4}$$

Given that the true signal transmission time at the BS, t_{Tx}, and the signal reception time at the UE, t_{Rx}, differ from the measured times, T_{Rx} and T_{Tx}, owing to inherent inaccuracies, a clock bias correction term is introduced:

$$\begin{aligned} T_{Rx} &= t_{Rx} + \delta t_{UE} \\ T_{Tx}^{BS\ i} &= t_{Tx}^{BS\ i} + \delta t_{Tx}^{BS\ i} \end{aligned} \tag{5}$$

Accordingly, it is possible to obtain the measurement $P_{UE}^{BS\ i}$:

$$P_{UE}^{BS\ i} = \left(T_{Rx} - T_{Tx}\right) \times c = \left[\left(t_{Rx} - t_{Tx}^{BS\ i}\right) + \left(\delta t_{UE} - \delta t_{Tx}^{BS\ i}\right)\right] \times c, \quad \forall i \in \{1, 2, \ldots, M\} \tag{6}$$

However, this model offers a simplified solution compared with reality: the TOA measurements are also affected by multipath and UE noise, which can generally be represented by the term v_i. The final pseudorange notation is as follows:

$$P_{UE}^{BS\ i} = \rho_{UE}^{BS_i} + \left[\delta t_{UE} - \delta t_{Tx}^{BS\ i}\right] \times c + v_i, \quad \forall i \in \{1, 2, \ldots, M\} \tag{7}$$

where ν_i is a generic term absorbing all other errors besides clock biases. We assume that $\delta t_{Tx}^{BS\ i}$ is known from the network. Thus, it is possible to estimate the UE's position and clock offset with at least four TOA measurements available. The assumption that BS biases are known is based on the fact that they are typically equipped with GNSS receivers for clock synchronization (Brambilla et al., 2024; Tedeschini et al., 2023). This allows for the compensation of timing biases with an accuracy similar to that of GNSS positioning. Looking forward, as 5G and future 6G networks evolve, network synchronization is expected to improve significantly, and timing biases may become known and broadcast as part of the system design—just as GNSSs currently share satellite clock and ephemeris data.

2.2 | LEO-PNT Positioning

Here, the term "LEO-PNT" refers to a satellite-based system designed to enhance PNT services. Unlike traditional GNSSs that operate in medium Earth orbit, LEO satellites operate in low Earth orbit, typically at altitudes of 400–2000 km, with an average velocity ranging from 7 to 8.5 km/s (Ries et al., 2023). As previously mentioned, the lower orbit allows for stronger signals, reduced latency, and faster changes in signal geometry. These features enable a LEO-PNT system to provide more reliable coverage, especially in urban canyons and challenging environments, by leveraging a larger constellation of satellites and advanced signal processing techniques (More et al., 2022). All of these benefits will lead to improvements in the accuracy, availability, and reliability of PNT services (Ferre & Lohan, 2021). At present, there are still no operational LEO-PNT constellations. Therefore, in this work, an LEO constellation is simulated, based on the available literature, along with the observations transmitted to the UE for navigation purposes.

For LEO-PNT signals, as in GNSSs, carrier frequencies belonging to the L-band, which refers to the range of frequencies within the radio spectrum from 1 to 2 GHz, are used as the baseline. This band is selected in satellite navigation because of its favorable propagation characteristics. In particular, all of the GNSS constellations are multi-frequency L-band systems; consequently, the GNSS can transmit multiple signals on different carrier frequencies, and the allocation of the frequency spectrum is managed by the International Telecommunication Union. Additional frequency bands, with regional navigation satellite system allocation, such as portions of the S-band or C-band, e.g., between 5.01 and 5.03 GHz, are also considered in some LEO-PNT initiatives.

In our work, we assume that LEO-PNT satellites, as in GNSS, are multi-frequency and can transmit on at least two different carrier frequencies: L1 and L9. The L1 band is the standard and oldest GNSS frequency band in use, typically ranging from 1559 MHz to 1610 MHz. This frequency band is used by most satellite navigation systems, including GPS, Galileo, BeiDou, satellite-based augmentation systems, and the Quasi-Zenith Satellite System. In the context of GLONASS, the L1 signal falls within a slightly different frequency range, typically around 1598.062–1605.375 MHz. L9 is the same as in the Navigation Indian Constellation, with a frequency of 2492.028 MHz.

The nonlinear code observation equation for a LEO constellation L of $l = 1, \ldots, n$ satellites at the time of observation t is as follows:

$$P_{UE}^{l}(t) = \rho_{UE}^{l}(t) + T_{UE}^{l}(t) + I_{UE}^{l}(t) + c\left[dt_{UE}^{L,f}(t) - dt^{l}(t)\right] + \nu_i(t) \tag{8}$$

In this study, the code observations were simulated according to the standard literature (Teunissen & Montenbruck, 2017) using a simplified model that does not include the satellite clock bias but its residual error (as shown below), because it is provided by the satellite itself, or the ionospheric error, because, as for GNSSs, we are processing the ionosphere-free observation in this work. Considering an epoch t and two observations from satellite s on frequencies A and B, it is possible to calculate the corresponding ionosphere-free observation as follows:

$$P^{l}_{UE,IF}(t) = \rho^{l}_{UE}(t) + T^{l}_{UE}(t) + c\left[dt^{L}_{UE,IF}(t) + dt^{l,IF}(t)\right] + \nu_{i}(t) \tag{9}$$

The tropospheric dry delay is modeled via the same standard models mentioned for GNSS processing (Hobiger & Jakowski, 2017).

2.3 | Hybrid Positioning Model

In the proposed work, we explore combining 5G, GNSS, and LEO-PNT technologies for positioning services, focusing on challenging environments such as urban and residential areas. The approach involves jointly processing 5G TOAs, LEO-PNT ionosphere-free pseudoranges, and GNSS pseudoranges in the ionosphere-free combination using an EKF (Evensen, 2007; Kalman, 1961; Sanso' et al., 2024). The EKF is specifically designed to estimate the receiver's position $\mathbf{X}_{UE} = [x, y, z]$, where x, y, and z are the global Cartesian coordinates of the user, along with the unknown clock offset parameters. The state vector of the proposed EKF solution is as follows:

$$\underline{\boldsymbol{x}} = \begin{bmatrix} \underline{\boldsymbol{X}}_{UE} \\ \underline{\boldsymbol{dt}}_{UE} \end{bmatrix} \tag{10}$$

where $\mathbf{dt}_{UE}$ is the the vector of the clock offsets of the receiver (multiplied by c) with respect to the different satellite constellations and the 5G system. According to the standard notation for an EKF, the model dynamic of the state vector is as follows:

$$\underline{\boldsymbol{x}}_{t} = \boldsymbol{T}_{t}\underline{\boldsymbol{x}}_{t-1} + \underline{\varepsilon}_{t} \tag{11}$$

where $\boldsymbol{T}_{t}$ is the state transition matrix. In the following, we assume that the model is nearly static, i.e., $\underline{\boldsymbol{x}}_{t} = \underline{\boldsymbol{x}}_{t-1} + \underline{\varepsilon}_{t}$; this implies that $\boldsymbol{T}$ is the identity matrix for all epochs. Notably, the model can be easily generalized to represent a kinematic model by introducing a constant velocity or even a constant acceleration assumption. $\underline{\varepsilon}_{t}$ is the model error: it is assumed to be normally distributed with zero mean and a diagonal covariance matrix $\boldsymbol{C}^{\varepsilon}_{t}$. The first three elements of $\boldsymbol{C}^{\varepsilon}_{t}$ represent the X, Y, Z positional state variances, which are assumed to be equal and denoted as $\sigma^{2}_{e_x}$. The following elements are the state variance of all clock offsets, again set to be equal and denoted as $\sigma^{2}_{e_t}$. The adopted values are specified in Table 1: these values are indeed arbitrary but have been selected based on reasonable assumptions for static or slowly dynamic scenarios (e.g., pedestrian motion). At epoch t, the measurement vector $\underline{\boldsymbol{Y}}_{t}$ contains GNSS and LEO ionosphere-free observations and 5G TOA observations. This vector can be written as follows:

$$\underline{\boldsymbol{Y}}_{t} = \boldsymbol{h}_{t}\left(\underline{\boldsymbol{x}}_{t}\right) + \underline{\nu}_{t} \tag{12}$$

TABLE 1
Model Standard Deviations

σ_{e_x}	σ_{e_t}
$1\ m$	$10\ m$

where $\boldsymbol{h}_t(\cdot)$ is a nonlinear vector function containing the observation equations, given by Equations (1), (7), and (9), and $\boldsymbol{\nu}_t$ is the observation error, which is assumed to be Gaussian with zero mean. For GNSS observations, standard values from the literature can be used (Herrera et al., 2016). For LEO-PNT, we assume a standard deviation of 1 m: this assumption is arbitrary but conservative and consistent with respect to GNSS standards. Moreover, GNSS and LEO observations are weighted by the elevations of the satellites: $\sigma^2_{OBS_i} \propto \frac{1}{\sin(El_i)}$. For 5G, the standard deviation of the observations is computed empirically, based on available measurements, as discussed in Section 4. The EKF is an adaptation of the Kalman filter designed to handle nonlinear systems, as, in our case, for the observation model. The equations must be linearized around an approximate value of the state vector: this value could be, for example, the prediction from the previous epoch, denoted as $\hat{\underline{\boldsymbol{x}}}_{t|t-1}$. To linearize the observed pseudodistances or TOAs between the receiver and satellites (or BSs), we follow the standard approach described by Odijk (2017). The resulting Jacobian includes partial derivatives with respect to the receiver position and clock biases:

$$\boldsymbol{H}_t = \left.\frac{\partial \boldsymbol{h}(\boldsymbol{x})}{\partial \boldsymbol{x}}\right|_{\boldsymbol{x}=\hat{\boldsymbol{x}}_{t|t-1}} \tag{13}$$

The final linearized observation model is as follows:

$$\underline{\boldsymbol{Y}}_t = \boldsymbol{h}_t\left(\hat{\underline{\boldsymbol{x}}}_{t|t-1}\right) + \boldsymbol{H}_t\left(\underline{\boldsymbol{x}}_t - \hat{\underline{\boldsymbol{x}}}_{t|t-1}\right) + \underline{\boldsymbol{\nu}}_t \tag{14}$$

In particular, our observations are already linear with respect to the unknown clock offsets, whereas the distance term must be linearized with respect to the UE coordinates:

$$\rho^i_{\underline{\boldsymbol{x}}_t} = \rho^i_{\hat{\underline{\boldsymbol{x}}}_{t|t-1}} + \underline{\boldsymbol{e}}^i_{\hat{\underline{\boldsymbol{x}}}_{t|t-1}}\left(\underline{\boldsymbol{x}}_t - \hat{\underline{\boldsymbol{x}}}_{t|t-1}\right) \tag{15}$$

where $\underline{\boldsymbol{e}}^i_{\hat{\underline{\boldsymbol{x}}}_{t|t-1}}$ is the unitary vector from emitter i to the approximate position of the user. The Kalman filtering proceeds as follows. At epoch 0, the state vector $\hat{\underline{\boldsymbol{x}}}_0$ is estimated by the available observations, and the covariance matrix $\boldsymbol{C}^{\eta}_0$ of the estimate is computed. For each following epoch t, the state vector is firstly predicted as follows:

$$\hat{\underline{\boldsymbol{x}}}_{t|t-1} = \boldsymbol{T}\underline{\boldsymbol{x}}_{t-1} + \underline{\boldsymbol{\varepsilon}}_t \tag{16}$$

The prediction covariance matrix is computed as follows:

$$\boldsymbol{C}_{\boldsymbol{x}_{t|t-1}} = \boldsymbol{T}\boldsymbol{C}^{\eta}_{t-1}\boldsymbol{T}^T \tag{17}$$

Then, the prediction is used to compute the linearized observation equations (Equation (15)); the estimate at epoch t is finally obtained by updating the prediction with the contribution of the observations at epoch t:

$$\underline{\hat{\boldsymbol{x}}}_{t|t} = \left(\boldsymbol{I} - \boldsymbol{G}_t \boldsymbol{H}_t\right) \underline{\hat{\boldsymbol{x}}}_{t|t-1} + \boldsymbol{G}_t \underline{\boldsymbol{y}}_t \tag{18}$$

where:

$$\boldsymbol{G}_t = \boldsymbol{K}_t \boldsymbol{H}_t \left(\boldsymbol{H}_t \boldsymbol{K}_t \boldsymbol{H}_t^T + \boldsymbol{C}_t^{\nu}\right)^{-1} \tag{19}$$

$$\boldsymbol{K}_t = \boldsymbol{C}_t^{\epsilon} + \boldsymbol{C}_{\boldsymbol{x}_{t|t-1}} \tag{20}$$

Finally, the covariance matrix of the estimate is computed:

$$\boldsymbol{C}_t^{\eta} = \left(\boldsymbol{I} - \boldsymbol{G}_t \boldsymbol{H}_t\right) \boldsymbol{K}_t \tag{21}$$

This process is iterated for all epochs and allows accurate position estimates to be provided even in the presence of nonlinearities in the system.

To provide a complete understanding of the implemented algorithm, Figure 3 presents a software flowchart, highlighting the process through which the observations are acquired or generated and processed in the Kalman filter. Further information about data acquisition is provided in Section 3.

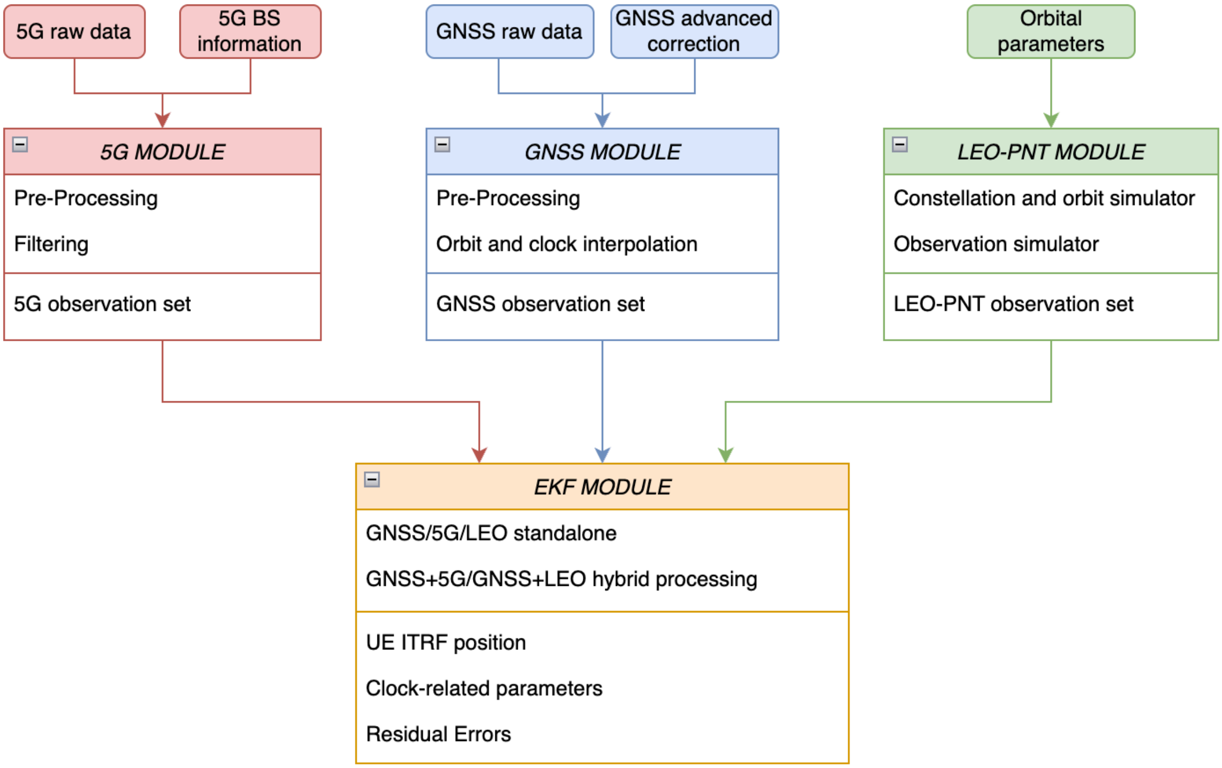

FIGURE 3 Hybrid software flowchart
ITRF: International Terrestrial Reference Frame

3 | EXPERIMENTAL METHODOLOGY

5G and GNSS data were acquired during field measurements performed as part of an experimental campaign carried out in the framework of the HYPER-5G project, funded by ESA's Navigation Innovation and Support Program and implemented by a consortium comprising G-RED, Politecnico di Milano, and AlgoWatt Italia. More details about this work have been reported by Brambilla et al. (2024). The LEO-PNT data were generated in a simulator, as described in Section 3.2.

3.1 | 5G and GNSS Data Acquisition

This site for the experimental activities was identified in a industrial area in southwestern Milan with open-sky conditions. This location was selected because of the favorable distribution of 5G cell towers in the area. Figure 4 shows the location of the measurement site, the transmitting BSs, and the relative distances with respect to the chosen site. From a horizontal dilution of precision (HDOP) analysis, shown in Figure 5, it is evident that the reception point is in the optimal area with a minimum HDOP value.

As discussed by Brambilla et al. (2024), the precise positions of all radio BSs of interest were determined from an RTK survey (two-dimensional location) and accurate drawings of the site (for antenna height), targeting a decimeter level of

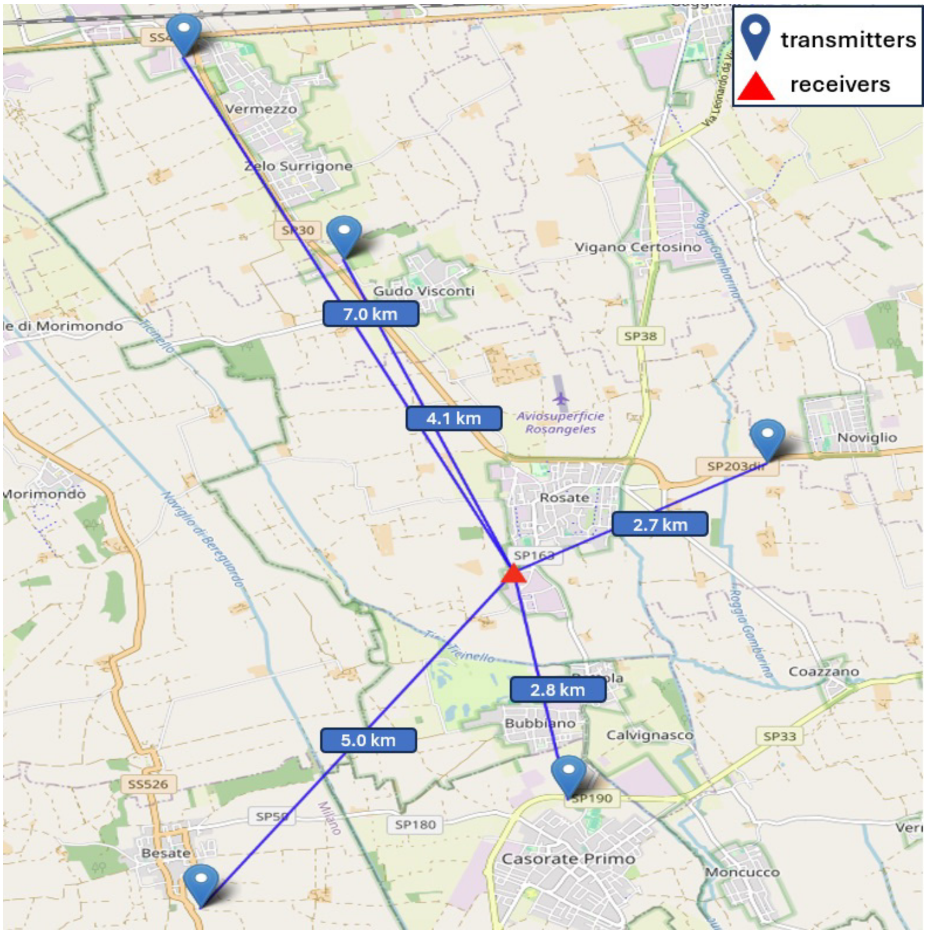

FIGURE 4 Distribution of transmitting BSs at the measurement site

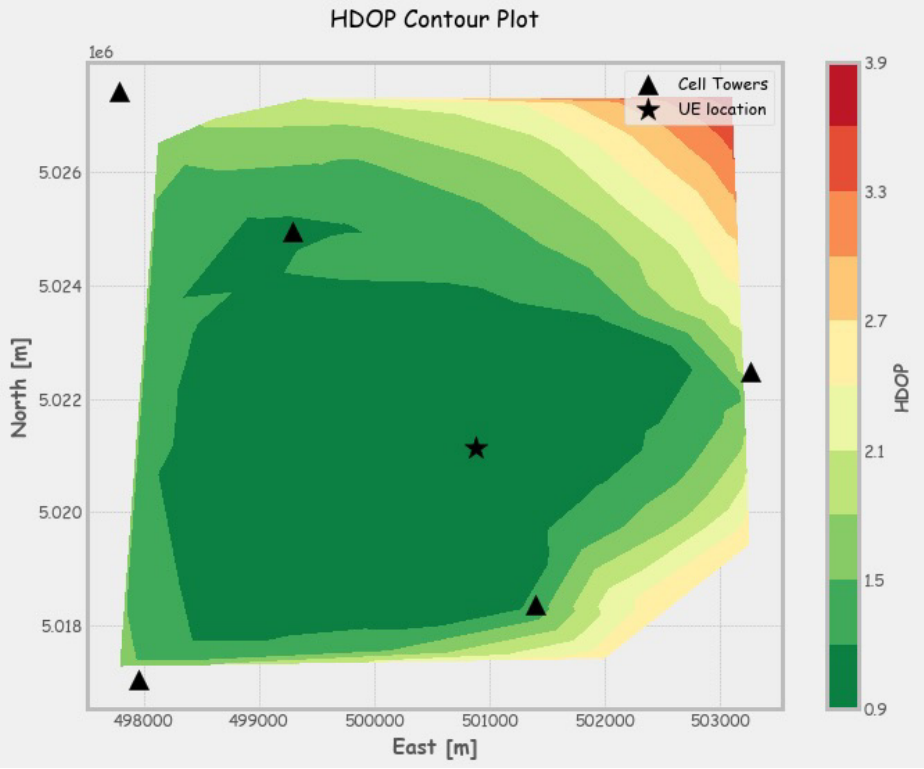

FIGURE 5 HDOP analysis of the area of interest with respect to the 5G network deployment

accuracy. Importantly, in a network, each device has its own clock, and all of the clocks must be synchronized to a common time reference to ensure an optimal operation of functions. In this case, the BSs are synchronized following Precision Time Protocol v2, which utilizes a master-slave architecture that allows the synchronization of secondary clocks to the reference time provided by the master clock, typically a GNSS receiver.

For the collection of 5G TOA measurements, a Rohde & Schwarz (R&S) TSME6 scanner was used. The R&S TSME6 is a passive network scanner equipped with a radio-frequency omnidirectional antenna, an embedded GNSS receiver, and a laptop running the ROMES4 software for command and control. ROMES4 was used also for real-time inspection of ongoing measurements and for exporting the collected data (e.g., TOA, reference signal received power, etc.) at the end of the measurement session. The GNSS receiver was used for geolocating and time-stamping the collected TOA measurements and for steering the scanner clock through an accurate pulse-per-second signal.

The GNSS equipment under test consists of an ALBICILLA receiver (Magellan Systems Japan) connected to an ANT3B-HEL antenna. The ground truth is obtained from an RTK solution based on the STONEX SG70 receiver and STONEX SA65 antenna. According to the receiver manufacturer, the final accuracy is 2 cm when in open-sky conditions.

The experimental campaign took place in May 2023 and consisted of eight static sessions, lasting approximately 5 min each, and seven kinematic tests.

3.2 | Generation of LEO-PNT Observables

The LEO-PNT constellation simulated for this work corresponds to the Walker constellation with three different inclinations; orbital parameters are reported in

Table 2. Figure 6 shows a skyplot of the available LEO-PNT satellites, tracking their positions over a 5-min time period for the considered obstructed environment (20° cutoff). The satellite positions were computed with respect to the location of the experimental activities. The 5-min duration corresponds to the measurement session length. More details are given below. For the observable simulation, we followed the same procedure as Perez et al. (2024). We conducted our analysis in the prefit residual stage, meaning that we modeled and assessed the residual errors associated with each observable before applying corrections:

$$\boldsymbol{Prefit} = \boldsymbol{dt}_{rec} + \boldsymbol{T}_{wet} \cdot \boldsymbol{M}_{wet} + \varepsilon_{\boldsymbol{CLOCK}} + \varepsilon_{\boldsymbol{LEO}} + \sigma_{\boldsymbol{OBS}} \tag{22}$$

The different simulated error components are σ_{OBS} and ε_{LEO}.σ_{OBS} corresponds to the thermal noise and multipath of the receiver. In this case, the multipath corresponds to Gaussian noise with an elevation dependency. For ε_{CLOCK}, the residual error is applied by a random walk process with a standard deviation of 12.5 cm and a Gaussian aoise with a standard deviation of 3 mm. For ε_{LEO}, the three components (radial, along-track, and cross-track) are affected by a random walk bias

TABLE 2
Different Inclination Constellations Used in the LEO-PNT Data The Walker type is given by N/P/F, where N is the number of satellites, P is the number of planes, and F is the phase.

Height	Inclination	Walker Type
975 *km*	55°	120/12/1
1125 *km*	87.4°	30/3/1
1050 *km*	30°	40/4/1

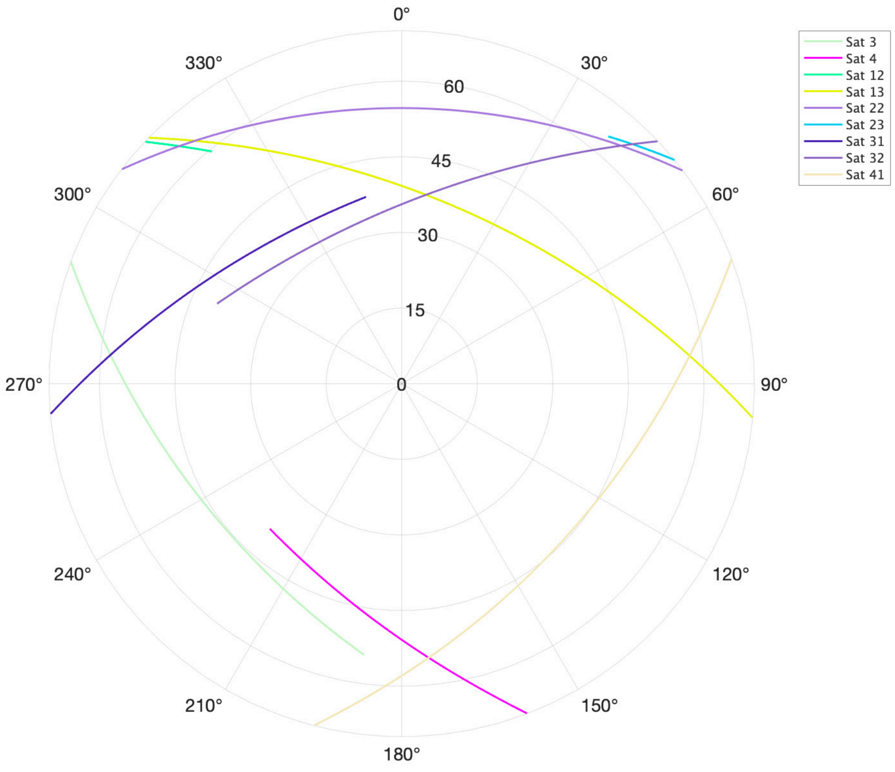

FIGURE 6 Skyplot of the LEO-PNT satellites, computed with respect to the test-site position, for a period of 5 min, considering a cutoff angle of 20°

in each direction with a standard deviation of 7.5 cm. This error not only affects the line of sight (LoS) but also the unitary vectors from the receiver to the satellite in view.

4 | RESULTS

Two hybridization scenarios are proposed to highlight the strengths of the technologies considered, namely, GNSS, LEO-PNT, and 5G. Additionally, the results of four (*A*, *B*, *C*, *D*) of the eight total tests conducted are discussed in detail. To simulate both open-sky and urban scenarios, we first tested the satellite visibility. Specifically, for GNSSs, we included satellites from GPS, Galileo, and BeiDou for which double-frequency observations are available, enabling an ionosphere-free combination. The cutoff representing the open-sky scenario is set to 5°. To simulate obstructed scenarios, we increased the cutoff. For a cutoff of 20°, the number of visible LEO-PNT satellites decreases drastically (see Table 3). Thus, in the present work, we kept the maximum cutoff at 20°, even if this scenario does not represent severe obstructions. In future work, different LEO constellation configurations will be investigated to optimize PNT services for taller obstructions. In addition, lower and faster LEO-PNT orbits cause faster changes in geometry, which reduce the satellite's visibility time (horizon to horizon in approximately 10–15 minutes in open-sky conditions). Introducing a cutoff further reduces this period, causing each satellite to be visible for only a few minutes. As an example, Figure 7 shows the number of satellites in the LoS per epoch for test *A*, sampled at 1 Hz; here, the number of available LEO-PNT satellites frequently drops to as low as 3, resulting in poor system conditioning.

To highlight the improvements in terms of accuracy obtainable from the integration of GNSS, 5G, and LEO-PNT, different scenarios have been investigated:

1. **H1 - 5G standalone:** processing of the experimental 5G TOA.
2. **H2 - GNSS standalone:** processing of the experimental ionosphere-free GNSS code observations.
3. **H3 - LEO-PNT standalone:** processing of the simulated ionosphere-free LEO-PNT code observations.
4. **H4 - 5G + LEO-PNT:** joint processing of experimental 5G TOA and the simulated uncombined LEO-PNT code observations.
5. **H5: LEO-PNT + GNSS:** joint processing of experimental ionosphere-free LEO-PNT code observations and ionsphere-free GNSS code observations.

Each scenario is processed by the EKF, as discussed in Section 2.3. At each epoch, the state vector contains the coordinates and the clock offsets of the considered

TABLE 3
Average Number of Satellites in the LoS for Different Tests
Here, **GNSS** refers to the sum of available satellites from GPS, Galileo, and BeiDou constellations for which we have double-frequency observations and can perform ionosphere-free combinations.

Test	GNSS - open-sky	GNSS - cutoff 20°	LEO-PNT - open-sky	LEO-PNT - cutoff 20°
A	14	11	11	4
B	14	13	11	4
C	14	14	11	4
D	15	10	10	5

data source (GNSS, LEO, and 5G), and the observation vector contains the relevant presudoranges. Proper standard deviations must be attributed to build $\boldsymbol{C}_t^{\nu}$; for GNSS and LEO, these have been discussed in Section 2.3. For 5G, the standard deviations of the observations are empirically computed, based on the available measurements. Specifically, for each test session for each BS, the expected pseudoranges can be computed by the known positions of the BS and the estimated position of the receiver; then, the standard deviations of the residuals, e.g., the differences between the observed and predicted pseudoranges, are computed. Each test session lasts approximately 5 min, with at a sampling rate of 1 Hz, resulting in approximately 300 observations for each BS. This sample should be sufficient to ensure a consistent estimate of the measurements' standard deviation. As a graphical example, Figure 8 presents a time series of the residuals of all of the BSs in test A. Table 4 reports the values of all of the empirical standard deviations, which

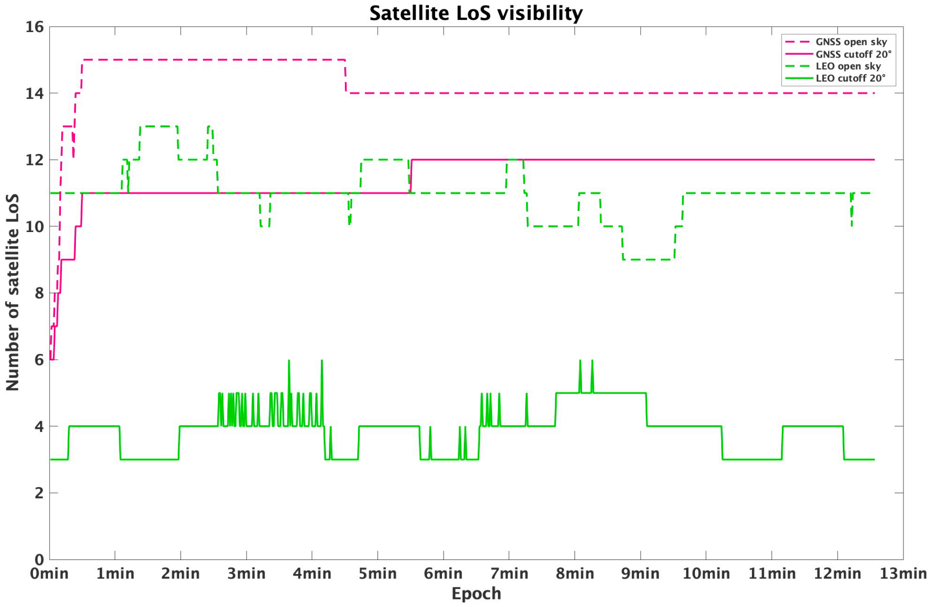

FIGURE 7 Average number of LoS satellites available at each epoch for test A
Here, **GNSS** refers to the sum of available satellites from GPS, Galileo, and BeiDou constellations for which we have double-frequency observations and can perform ionosphere-free combinations.

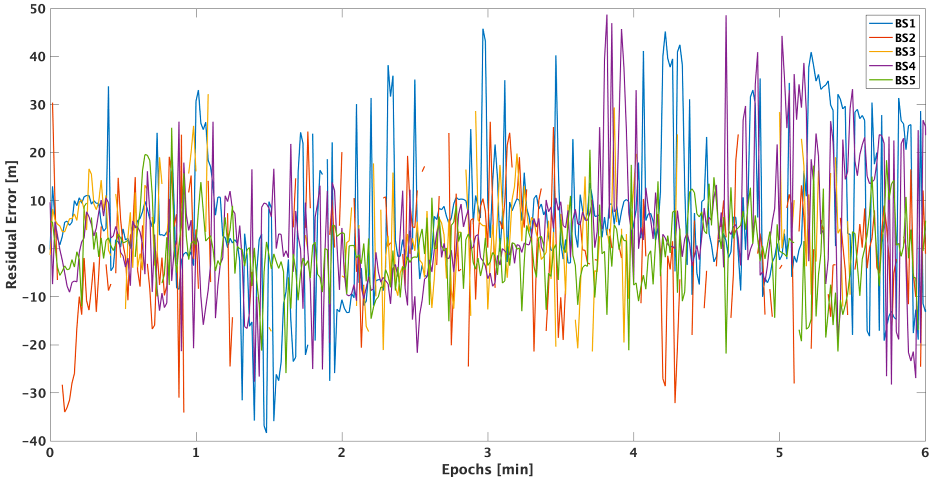

FIGURE 8 Residuals of 5G observations in test A

TABLE 4
Empirical Standard Deviations of the 5G Observations in Tests A–D

Test	BS1 [m]	BS2 [m]	BS3 [m]	BS4 [m]	BS5 [m]	BS6 [m]
A	15.1	12.4	10.7	13.3	7.6	15.4
B	2.77	12.3	3.09	14.7	11.3	13.3
C	8.75	11.3	6.29	5.43	7.29	11.7
D	2.98	14.0	2.93	14.0	5.22	9.33

TABLE 5
Statistical Analysis of the Different Processing Scenarios in an Urban Environment
Mean, standard deviation, and maximum value of the residual errors are presented for the east, north, and up components of the estimates of the different tests for a cutoff of 20°. Results are reported in meters.

		H1			H2			H3			H4			H5		
		E	N	U	E	N	U	E	N	U	E	N	U	E	N	U
A	**Mean**	−8.4	−0.8	195	1.5	0.7	1.5	1.8	0.4	−1.8	1.0	0.0	4.5	0.9	0.1	0.6
	Std	6.8	6.9	64	0.8	2.2	4.8	3.7	1.9	13	2.1	1.4	12	0.9	0.8	3.5
	Max	29	21	357	4.5	6.8	18	19	9.8	66	7.1	5.8	47	3.4	2.6	9.4
B	**Mean**	0.9	−1.6	65	1.4	0.4	3.7	−8.4	3.1	−14	0.5	0.2	−1.2	1.2	−0.1	2.0
	Std	4.2	4.3	69	1.1	1.8	6.7	11	3.7	17	3.6	1.8	12	1.0	0.9	4.7
	Max	16	14	266	4.8	5.4	18	27	10	67	13	6.8	48	4.0	2.2	12
C	**Mean**	0.1	−0.3	−19	1.1	1.1	1.9	−0.1	0.2	−1.0	0.0	0.3	−1.1	0.4	0.3	1.9
	Std	4.4	6.2	29	1.1	1.2	3.8	0.8	1.3	7.9	0.8	1.2	7.1	0.9	1.1	3.9
	Max	12	18	126	4.2	4.5	12	2.6	5.6	33	3.2	4.0	28	3.7	2.8	18
D	**Mean**	−16	−0.2	277	1.0	−1.5	2.7	−0.3	0.2	−0.6	−0.3	0.4	−1.0	0.1	0.2	0.9
	Std	8.9	6.3	50.5	1.4	3.4	6.4	0.9	0.9	6.2	1.0	1.0	6.7	0.9	0.9	4.4
	Max	41	17	411	4.2	8.7	18	4.2	8.7	18	4.1	3.3	22	3.4	2.9	13

are then adopted in the EKF. The residuals do not behave uniformly across sessions; BS1 and BS3 are the best in tests B and D but not in the others. This result does not seem to be attributable to variations in multipath because the sessions are always repeated in the same position and therefore in the same geometry.

Note that results for **H1** and **H2** have been extensively discussed by Brambilla et al. (2024). However, over the last months, new software has been developed and data have been reprocessed. The additional scenario **H6** (5G + LEO + GNSS) is not discussed in the following because the introduction of 5G alongside LEO and GNSS does not provide any significant benefit. This lack of benefit arises from the fact that 5G observations are heavily affected by multipath, as shown in Figure 8, resulting in high standard deviations for the observable, as reported in Table 4. When there is an adequate number of LEO and GNSS observations, their influence is dominant, and the 5G observations have less weight in the solution.

For scenario **H1**, we computed the residuals for the east, north, and up components of the estimates with respect to the corresponding ground truth. The statistical analyses of the results are summarized in Table 5. For a deeper analysis of the obtained results, we refer to the work of Brambilla et al. (2024). The results are noisy and affected by significant errors. As expected, the most critical component is the vertical component: it is impossible to accurately estimate the height owing to the geometry of the transmitting BS with respect to the UE. Specifically, all of the BSs have a height of approximately 50 m above ground; therefore, although

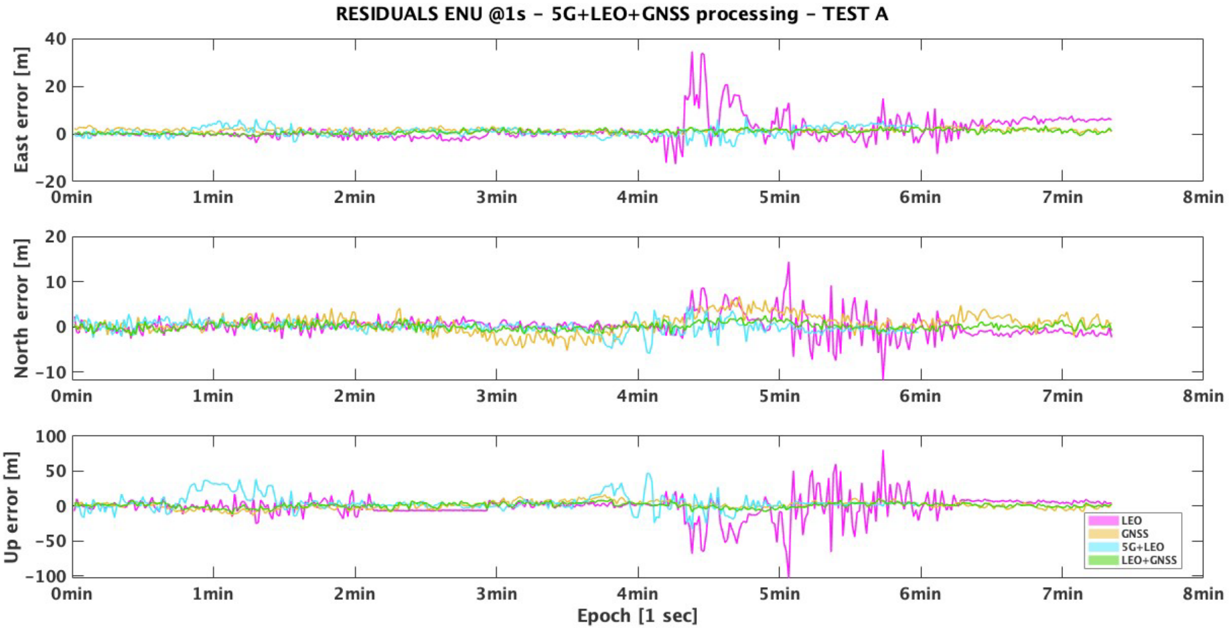

FIGURE 9 Residual errors in the east, north, and up (ENU) components for test A with a cutoff of 20°

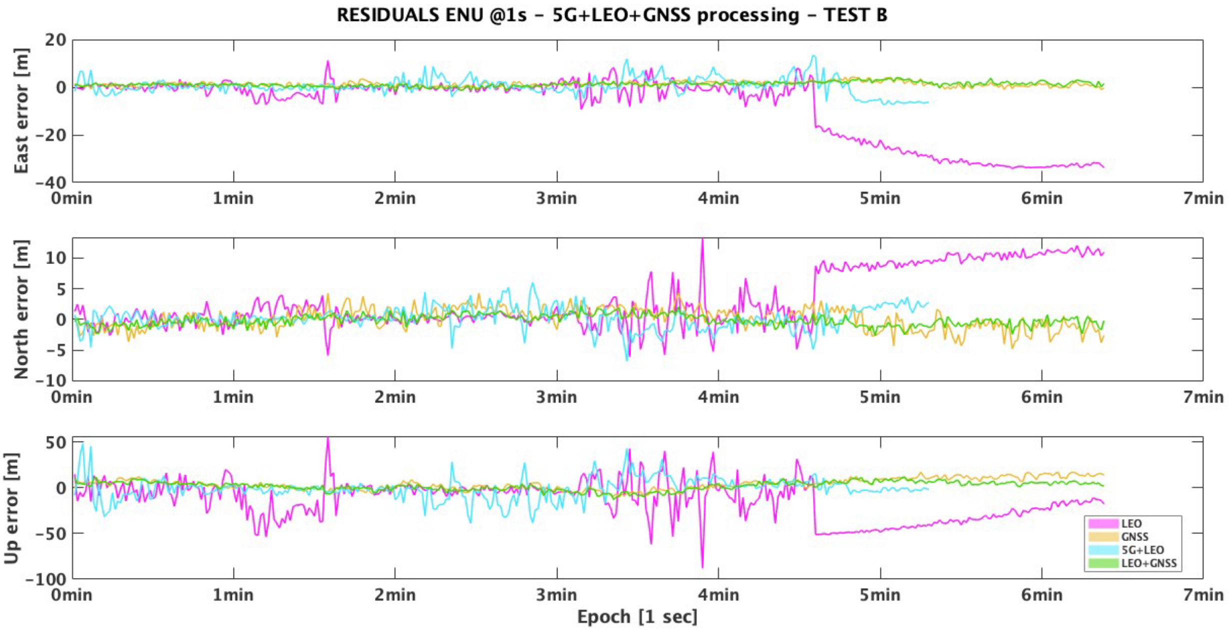

FIGURE 10 Residual errors in the east, north, and up components for test B with a cutoff of 20°

the HDOP values are favorable (Figure 5), the system is ill-conditioned and it is not possible to properly estimate the altitude. For the east and north components, the errors are reduced by approximately one order of magnitude but still remain too noisy and biased to be realistically applied for PNT services. Although the average errors in some tests can be small (Table 5), the respective standard deviations remain high. This result is also caused by the quality of the measured TOA, which is affected by multipath and noise. We note that the errors affecting the 5G observations, as discussed in Section 2.1, are not zero-mean Gaussian, primarily because

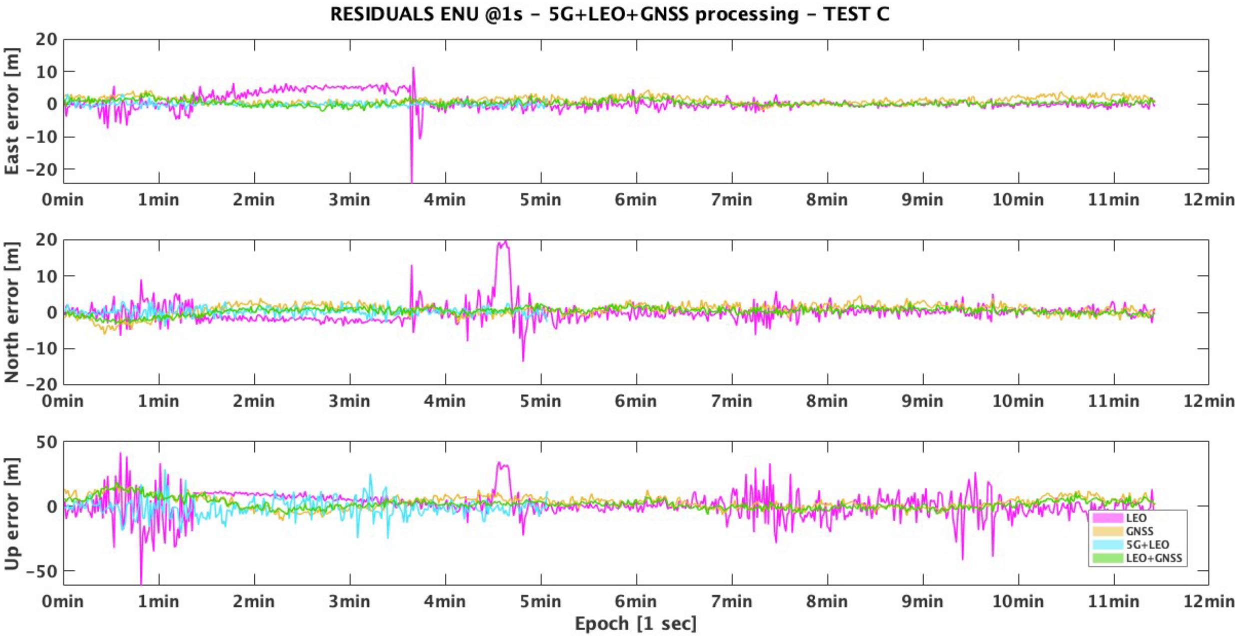

FIGURE 11 Residual errors in the east, north, and up components for test C with a cutoff of 20°

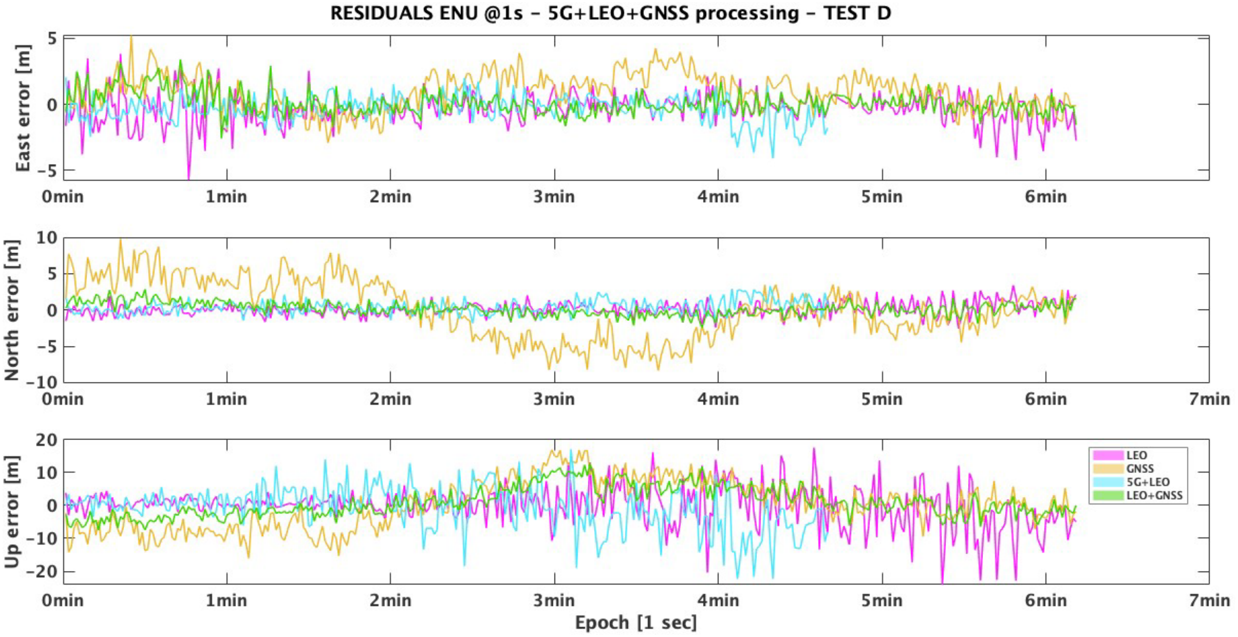

FIGURE 12 Residual errors in the east, north, and up components for test D with a cutoff of 20°

of multipath effects. Consequently, the application of a Kalman filter is statistically suboptimal; however, because this type of simplification is commonly applied in the processing of geomatic data, we chose to adopt it.

Focusing first on the urban environment scenario, Figures 9–12 show the residuals errors in the east, north, and up components of the estimated UE locations computed during the different tests. The different figures compare, for each test, the results obtainable from the different types of processing applied to the data sets for **H2**, **H3**, **H4**, and **H5**. The LEO standalone solution (**H3**) present significant

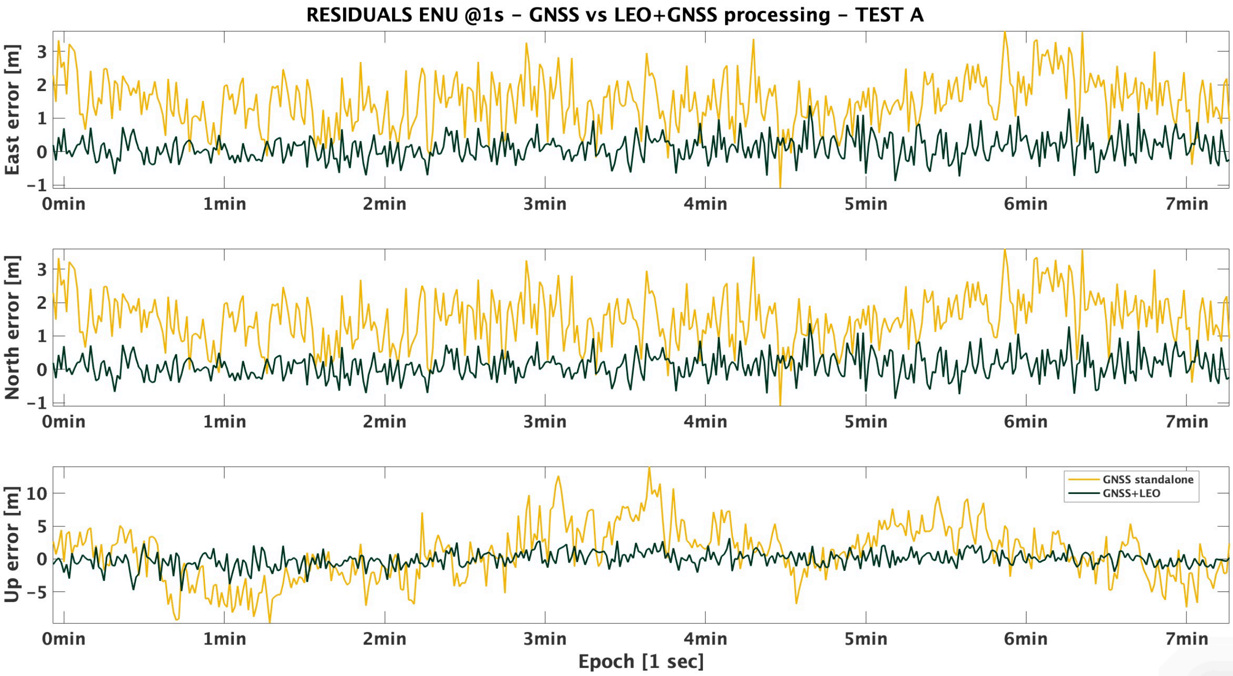

FIGURE 13 Residual errors in the east, north, and up components for test A with a cutoff of 5°

instabilities over time; for example, in test A (Figure 9), a clear degradation appears after approximately 4 min. This instability is primarily related to the change in satellite geometry; although approximately 3–4 LEO satellites are always in view, the setting of a satellite and its replacement by a newly risen satellite can cause an abrupt change in geometry, sometimes significantly for the worse. To highlight the improvements obtainable from the different integration methods, we report the results that we can obtain from configurations **H2** and **H3**, corresponding to GNSS and LEO-PNT standalone processing, respectively. The tested hybrid configurations are **H4** and **H5**, corresponding to 5G + LEO and LEO + GNSS, respectively. Statistical analyses (mean, standard deviation, and maximum value) are reported for all tests in Table 5. The results show that, first, the **H3** solution in an urban environment is dependent on and penalized by the poor visibility conditions of LEO-PNT satellites in orbit. As discussed earlier, the cutoff of 20° compromises the availability of satellites, resulting in epochs where only 2–3 satellites are in the LoS. This causes significant errors of up to 20 m in the UE position estimation. However, the introduction of 5G TOA in configuration **H4** allows for a significant reduction in errors during periods of poor satellite visibility, despite the 5G observations being noisy and affected by multipath. As shown, for example, in Figure 10, the **H4** solution remains stable and does not diverge, in contrast to the LEO standalone processing, where the solution diverges by several meters after approximately 4.5 min. The plots also display the positioning performance obtained with GNSS-only processing (**H2**); the obtained results are aligned with the expected accuracy achievable through standard code-based positioning. However, the hybrid GNSS + LEO configuration (**H5**) provides the best results in almost all tests: although the LEO satellites are limited in number, a clear enhancement in positioning accuracy is still observable.

To further analyze the improvements achievable through the integration of GNSS and LEO, the results obtained in open-sky conditions for scenarios **H2** and **H5** are discussed. Therefore, we adopted a cutoff of 5° to exclude the lowest and

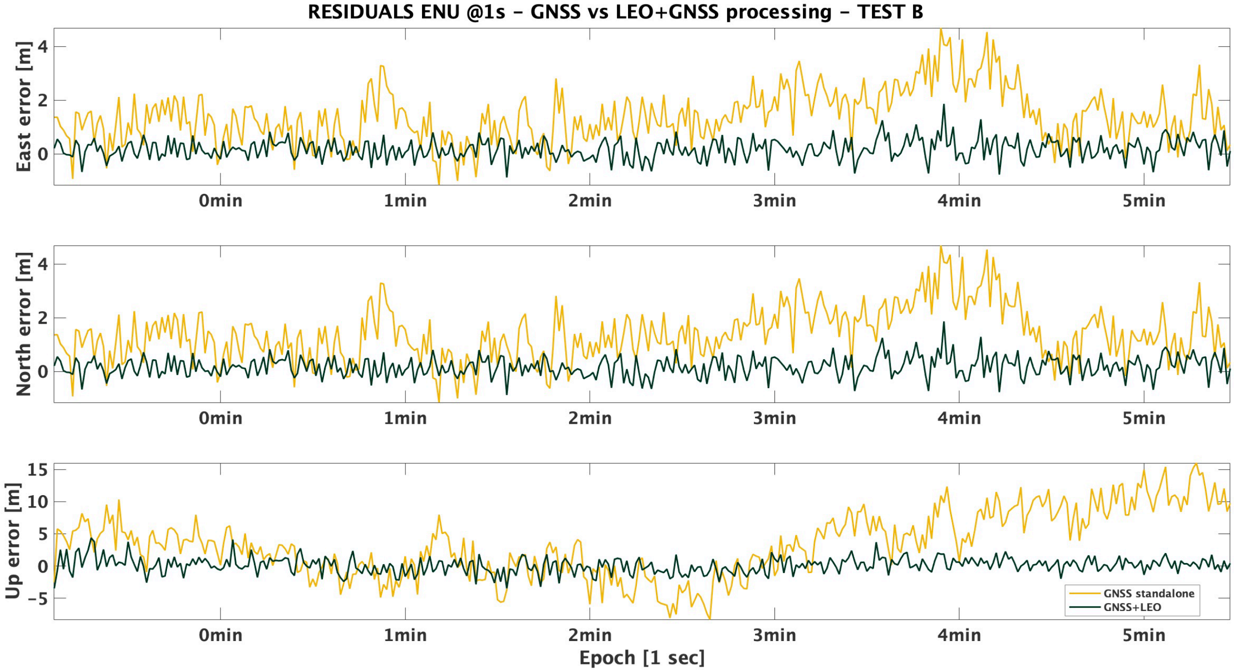

FIGURE 14 Residual errors in the east, north, and up components for test B with a cutoff of 5°

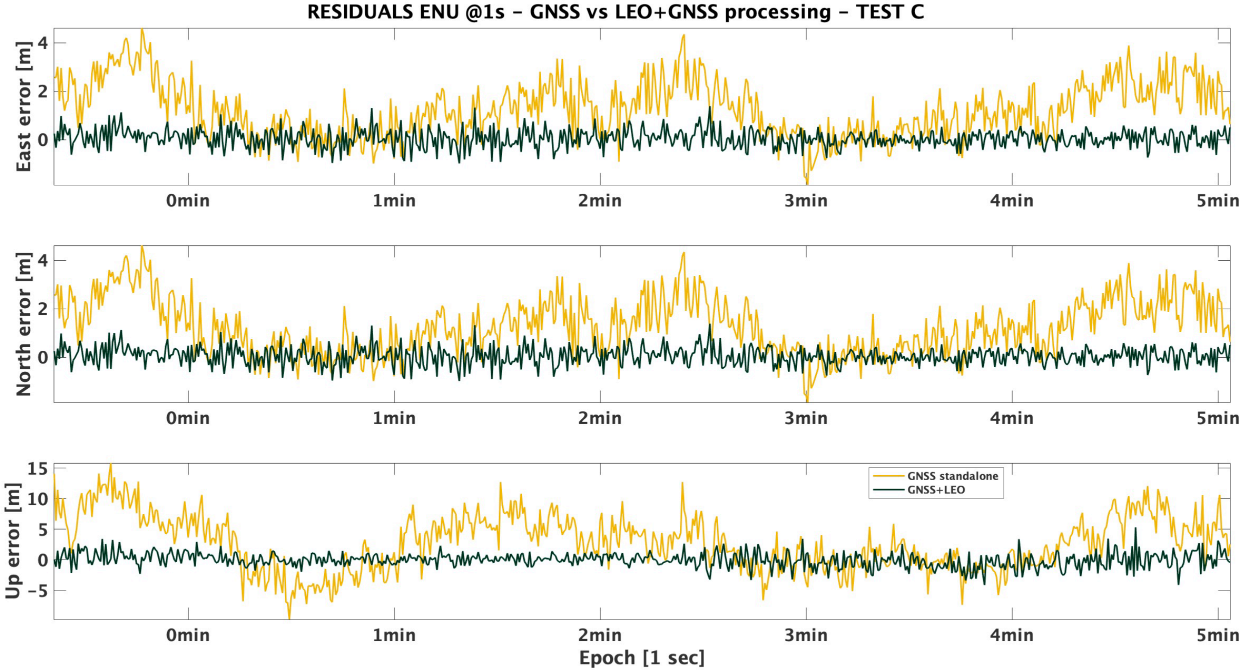

FIGURE 15 Residual errors in the east, north, and up components for test C with a cutoff of 5°

noisiest satellites. Figures 13–16 illustrate the east, north, and up residuals of the estimates compared with the benchmark results. It is evident that the introduction of additional LEO satellites stabilizes the solution, further reducing noise and potential errors. These findings are corroborated by the statistical analysis presented in Table 6.

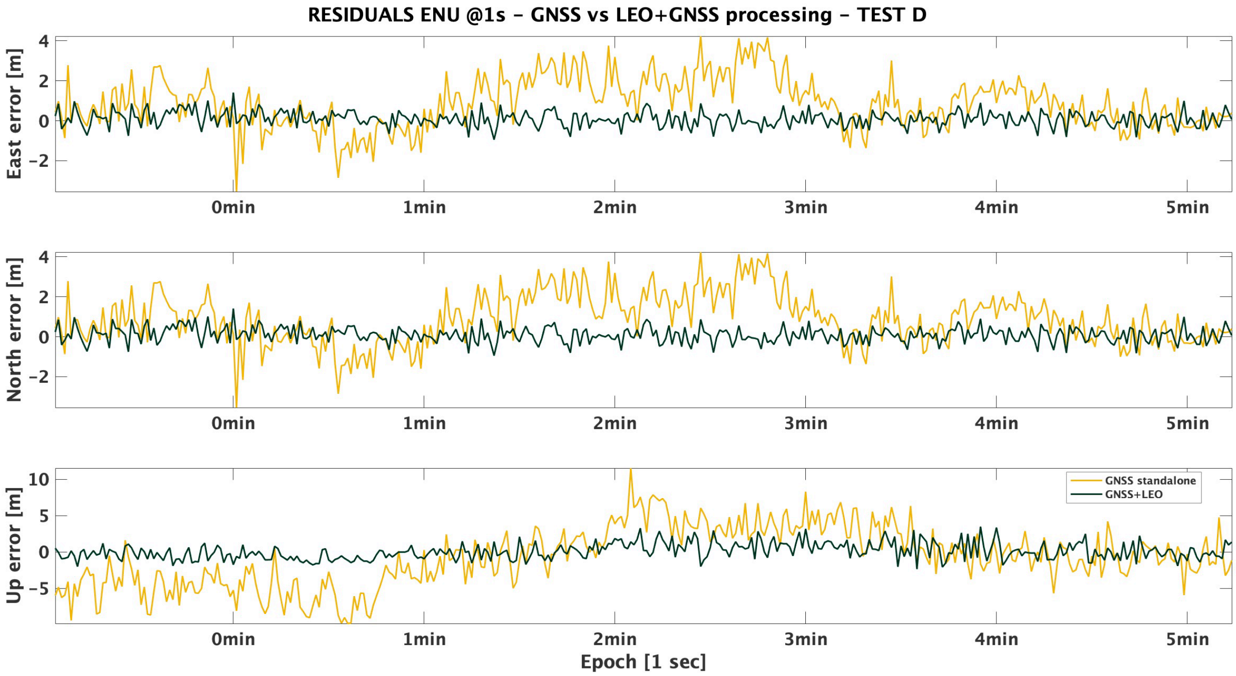

FIGURE 16 Residual errors in the east, north, and up components for test D with a cutoff of 5°

TABLE 6
Statistical Analysis of Scenarios **H2** and **H5** in Open-Sky Conditions
Mean, standard deviation, and maximum value of the residual errors are presented for the east, north, and up components of the estimates of the different tests for a cutoff of 5°.

		H2			H5		
		E	N	U	E	N	U
A	**Mean**	1.5	1.6	3.4	0.3	0.3	0.9
	Std	0.7	1.9	4.2	0.4	0.4	1.2
	Max	3.6	6.6	14	1.4	1.2	4.8
B	**Mean**	1.5	1.3	4.9	0.3	0.3	0.9
	Std	1.0	1.6	5.1	0.4	0.4	1.2
	Max	4.7	4.7	16	1.9	1.2	4.3
C	**Mean**	1.4	1.4	4.2	0.3	0.3	0.9
	Std	1.2	1.5	1.5	0.4	0.4	1.2
	Max	4.6	5.1	16	1.4	1.7	5.3
D	**Mean**	1.2	2.5	3.3	0.3	0.3	0.9
	Std	1.2	3.01	4.1	0.4	0.4	1.1
	Max	4.2	7.0	12	1.4	1.4	3.4

5 | CONCLUSIONS

This study has highlighted the potential of hybridization techniques to enhance GNSS positioning services. Among these techniques, the introduction of a LEO-PNT constellation is a promising solution, helping to achieve meter-level accuracy in two-dimensional error even in conditions of mediocre satellite geometry and availability. The promising results from LEO-PNT suggest that further testing with optimized constellations, specifically designed to improve visibility in dense urban areas, could yield even greater improvements in positioning accuracy. Although current 5G deployments are not yet capable of delivering high-precision positioning, they provide a useful backup solution in the short term, compensating for GNSS signal loss when it occurs. Future research should thus investigate the combined use of these hybrid techniques to achieve robust and precise positioning solutions tailored to urban environments.

ACKNOWLEDGMENTS

The processed 5G and GNSS data were collected within the framework of the HYPER-5G project. Special thanks are extended to the project partners G-RED and the IoT Lab of Politecnico di Milano for their collaboration and valuable support. We express our gratitude to the Navigation Directorate and, in particular, the LEO-PNT team of the ESA for providing hosting and research opportunities to the lead author at the European Space Research and Technology Centre, The Netherlands, from April 2024 to September 2024. Finally, the authors would like to thank the anonymous reviewers for their valuable suggestions, which have significantly contributed to improving the quality of this article.

REFERENCES

3rd Generation Partnership Project. (2017). *NG radio access network (NG-RAN); stage 2 functional specification of user equipment (UE) positioning in NG-RAN (release 15)* (Technical Specification (TS) 38.305) (Version 15.0.0). 3rd Generation Partnership Project (3GPP).

3rd Generation Partnership Project. (2020b). *NR; physical channels and modulation (release 16)* (Technical Specification (TS) 38.211) (Version 16.4.0). 3rd Generation Partnership Project (3GPP).

Abdallah, A., & Kassas, Z. (2022, March). Opportunistic navigation using sub-6 GHz 5G downlink signals: A case study on a ground vehicle [Special session]. In *Proceedings of the European Conference on Antennas and Propagation (EuCAP)* (pp. 1–5). https://doi.org/10.23919/eucap53622.2022.9769276

Alghisi, M., & Biagi, L. (2023). Positioning with GNSS and 5G: Analysis of geometric accuracy in urban scenarios. *Sensors*, *23*(4), 2181. https://doi.org/10.3390/s23042181

Brambilla, M., Alghisi, M., Tedeschini, B. C., Fumagalli, A., Grec, F. C., Italiano, L., Pileggi, C., Biagi, L., Bianchi, S., Gatti, A., Goia, A., Nicoli, M., & Realini, E. (2024). Integration of 5G and GNSS technologies for enhanced positioning: An experimental study. *IEEE Open Journal of the Communications Society*, *1*, 59–65. https://doi.org/10.1109/OJCOMS.2024.3487270

Chaloupka, Z. (2017). Technology and standardization gaps for high accuracy positioning in 5G. *IEEE Communications Standards Magazine*, *1*(1), 59–65. https://doi.org/10.1109/MCOMSTD.2017.1601030ST

del Peral-Rosado, J. A., Saloranta, J., Destino, G., López-Salcedo, J. A., & Seco-Granados, G. (2018). Methodology for simulating 5G and GNSS high-accuracy positioning. *Sensors*, *18*(10), 3220. https://doi.org/10.3390/s18103220

Dwivedi, S., Shreevastav, R., Munier, F., Nygren, J., Siomina, I., Lyazidi, Y., Shrestha, D., Lindmark, G., Ernstrom, P., Stare, E., et al. (2021). Positioning in 5G networks. *IEEE Communications Magazine*, *59*, 38–44. https://arxiv.org/abs/2102.03361

Evensen, G. (2007). *Data assimilation: The ensemble Kalman filter*. Springer Verlag.

Farahsari, P. S., Farahzadi, A., Rezazadeh, J., & Bagheri, A. (2022). A survey on indoor positioning systems for IoT-based applications. *IEEE Internet of Things Journal*, *9*(10), 7680–7699. https://doi.org/10.1109/JIOT.2022.3149048

Federal Communication Commission (FCC). (1996). *Report and order and further notice of proposed rulemaking on revision of the FCC rules to ensure compatibility with enhanced 911 emergency calling systems* (tech. rep.). Federal Communications Commission. Washington, DC, USA.

Ferre, R. M., & Lohan, E. S. (2021). Comparison of MEO, LEO, and terrestrial IoT configurations in terms of GDOP and achievable positioning accuracies. *IEEE Journal of Radio Frequency Identification*, *5*(3), 287–299. https://doi.org/10.1109/JRFID.2021.3079475

Fisher, S. (2021). 5G NR positioning. In X. Lin & N. Lee (Eds.), *5G and beyond, fundamentals and standards*. Springer.

Herrera, A.M., Suhandri, H.F., Realini, E., Reguzzoni, M., & de Lacy, M.C. (2016). goGPS: Open-source MATLAB software. *GPS Solutions*, *20*, 595–603. https://doi.org/10.1007/s10291-015-0469-x

Hobiger, T., & Jakowski, N. (2017). Atmospheric signal propagation. In P. Teunissen & O. Montenbruck (Eds.), *Springer handbook of global navigation satellite systems* (pp. 165–193). Springer International Publishing.

Italiano, L., Tedeschini, B. C., Brambilla, M., Huang, H., Nicoli, M., & Wymeersch, H. (2024). A tutorial on 5G positioning. *IEEE Communications Surveys & Tutorials*, *27*, 1488–1535. https://doi.org/10.1109/COMST.2024.3449031

Kalman, R. E. (1961). A new approach to linear filtering and prediction theory. *Transactions of the ASME–Journal of Basic Engineering*, *83*, 95–107.

Koivisto, M., Costa, M., Werner, J., Heiska, K., Talvitie, J., Leppänen, K., Koivunen, V., & Valkama, M. (2017). Joint device positioning and clock synchronization in 5G ultra-dense networks. *IEEE Transactions on Wireless Communications*, *16*(5), 2866–2881. https://doi.org/10.1109/TWC.2017.2669963

Leick, A., Rapoport, L., & Tatarnikov, D. (2015). *GPS satellite surveying* (4th ed.). Wiley.

Li, M., Xu, T., Guan, M., Gao, F., & Jiang, N. (2022). LEO constellation augmented multi-GNSS real-time PPP for rapid reconvergence in harsh environments. *GPS Solutions*, *26*, article no. 29. https://doi.org/10.1007/s10291-021-01217-9

Li, W., Yang, Q., Du, X., Min, L., Zhao, Q., Yang, L., Qin, Y., Chang, C., Wang, Y., & Qin, G. (2024). LEO augmented precise point positioning using real observations from two centispace experimental satellites. *GPS Solutions*, *28*, article no. 44. https://doi.org/10.1007/s10291-023-01589-0

Mata, F.J., Grec, F-C., Azaola, M., Blázquez, F., Fernández, A., Dominguez, E., Cueto-Felgueroso, G., Seco-Granados, G., del Peral-Rosado, J.A., Staudinger, E., Gentner, C., Kasparek, M., Backert, C., Barlett, D., Serna, E., Ries, L., & Prieto-Cerdeira, R. (2020, September). Preliminary field trials and simulations results on performance of hybrid positioning based on GNSS and 5G signal. In *Proceedings of the 33rd International Technical Meeting of the Satellite Division of the Institute of Navigation (ION GNSS+ 2020)* (pp. 387–401). https://doi.org/10.33012/2020.17609

More, H., Cianca, E., & Sanctis, M. D. (2022, October). Positioning performance of LEO mega constellations in deep urban canyon environments. In *2022 25th International Symposium on Wireless Personal Multimedia Communications (WPMC)* (pp. 256–260). https://doi.org/10.1109/WPMC55625.2022.10014853

Odijk, D. (2017). Positioning models. In P. Teunissen & O. Montenbruck (Eds.), *Springer handbook of global navigation satellite systems* (pp. 519–550). Springer. https://doi.org/10.1007/978-3-319-42928-1_17

Perez, R. O., Limon, M. C., Giordano, P., & Prieto-Cerdeira, R. (2024, October). Mixing real and simulated observables to assess the performance of hybrid GNSS/LEO-PNT precise positioning. In *Proceedings of the 37th International Technical Meeting of the Satellite Division of the Institute of Navigation (ION GNSS+ 2024)* (pp. 2308–2322). https://doi.org/10.33012/2024.19823

Pileggi, C., Grec, F. C., & Biagi, L. (2023). 5G positioning: An analysis of early datasets. *Sensors*, *23*(22), 9222. https://doi.org/10.3390/s23229222

Prol, F. S., Kaasalainen, S., Lohan, E. S., Bhuiyan, M. Z. H., Praks, J., & Kuusniemi, H. (2023, June). Simulations using LEO-PNT systems: A brief survey. In *2023 IEEE/ION Position, Location and Navigation Symposium (PLANS)* (pp. 381–387). https://doi.org/10.1109/PLANS53410.2023.10140118

Ries, L., Limon, M. C., Grec, F.-C., Anghileri, M., Prieto-Cerdeira, R., Abel, F., Miguez, J., Perello-Gisbert, J. V., D'Addio, S., Ioannidis, R., Ostillio, A., Rapisarda, M., Sarnadas, R., & Testani, P. (2023, October). LEO-PNT for augmenting Europe's space-based PNT capabilities. In *2023 IEEE/ION Position, Location and Navigation Symposium (PLANS)* (pp. 329–337). https://doi.org/10.1109/PLANS53410.2023.10139999

Ruffini, S., Johansson, M., Pohlman, B., & Sandgren, M. (2021). 5G synchronization requirements and solutions. *Ericsson Technology Review*, *2021*(1), 2–13. https://doi.org/10.23919/ETR.2021.9904655

Sanso', F., Pileggi, C., & Biagi, L. (2024). *A tutorial on Kalman filtering: The linear, extended and unscented filters* [Available: https://www.g-red.eu/]. GReD.

Shahcheraghi, S., Kuric, J., & Kassas, Z. (2024, September). Opportunistic positioning with beamformed 5G signals. In *Proceedings of the 37th International Technical Meeting of the Satellite Division of the Institute of Navigation (ION GNSS+ 2024)* (pp. 2522–2533). https://doi.org/10.33012/2024.19897

Singh, G. (2023). Satellite communication constellations as sources of alternate PNT (position, navigation, and timing). In *IET Conference Proceedings* (Vol. 2022, pp. 176–185). https://doi.org/10.1049/icp.2023.1383

Tedeschini, B. C., Brambilla, M., Italiano, L., Reggiani, S., Vaccarono, D., Alghisi, M., Benvenuto, L., Goia, A., Realini, E., Grec, F., & Nicoli, M. (2023). A feasibility study of 5G positioning with current cellular network deployment. *Scientific Reports*, *13*, art. no. 15281. https://doi.org/10.1038/s41598-023-42426-1

Teunissen, P., & Montenbruck, O. (Eds.). (2017). *Springer handbook of global navigation satellite systems* (1st ed.). Springer. https://doi.org/10.1007/978-3-319-42928-1

Vook, F. W., Ghosh, A., Diarte, E., & Murphy, M. (2018, October). 5G new radio: Overview and performance. In *2018 52nd Asilomar Conference on Signals, Systems, and Computers* (pp. 1247–1251). https://doi.org/10.1109/ACSSC.2018.8645228

Wymeersch, H., Seco-Granados, G., Destino, G., Dardari, D., & Tufvesson, F. (2017). 5G mmWave positioning for vehicular networks. *IEEE Wireless Communications*, *24*(6), 80–86. https://doi.org/10.1109/MWC.2017.1600374

Zhu, N., Marais, J., Bétaille, D., & Berbineau, M. (2018). GNSS position integrity in urban environments: A review of literature. *IEEE Transactions on Intelligent Transportation Systems*, *19*(9), 2762–2778. https://doi.org/10.1109/TITS.2017.2766768

How to cite this article: Alghisi, M., Grec, F-C., Orus Perez, R., & Biagi, L. (2026). Augmenting GNSS with LEO-PNT and 5G for enhanced positioning in urban environments. *NAVIGATION*, *73*. https://doi.org/10.33012/navi.770